

# Suitability of Graph Neural Network for Shape Memory Alloys

Stefan Bringuer<sup>✉,\*</sup>

<sup>a</sup>Independent Researcher, San Diego, CA, United States

---

## Abstract

Shape Memory Alloys (SMAs), such as NiTi, are crucial in vibration dampening, robotic arms, prosthetic hands, and mechanical valves due to their unique displacive phase transformation properties. However, assessing their phonon characteristics using conventional Density Functional Theory (DFT) methods is computationally expensive. This paper evaluates the use of recent Graph Neural Network (GNN) potentials as a viable alternative. These GNN potentials, trained on extensive DFT-computed databases, approximate potential energy surfaces, enabling inference on energies and forces in lattice and atomic dynamics calculations. We compare GNN potentials with the Embedded Atom Method (EAM) and Modified EAM (MEAM) potentials in predicting phonon properties of NiTi and PtTi. Generally, EAM/MEAM potentials appear to slightly outperform GNNs phonon, providing more accurate descriptions of the equation of state, phonon dispersions, and elastic constants. However, the MAE potential shows significant promise as an exploratory tool for designing and characterizing more complex SMAs. Our findings suggest GNN potentials as a promising initial avenue for advancing SMA research, particularly for ternary and quaternary systems, with improved outcomes possible by fine-tuning pre-trained GNN models with more relevant DFT data (e.g., force-constants).

*Keywords:* shape memory alloys, machine learning potentials, phonons

---

## 1. Introduction

The design and development of shape memory alloys (SMA) via *in-silico* methods would provide great value in advancing structural, medical, and other technologies. In order to enable such activity would require sampling from very large structural and compositional spaces and evaluating material properties indicative of displacive phase transformation phenomena. The use of density functional theory calculations to obtain properties such as equations of state,

---

\*Corresponding author

Email address: [stefanbringuer@gmail.com](mailto:stefanbringuer@gmail.com) (Stefan Bringuer<sup>✉</sup>)

phonon band structures, and elastic constants, can be done, however, such calculations are computationally demanding and are potentially prohibitive for smaller groups trying to develop new SMAs. To alleviate such restriction, one can resort to classical interatomic potentials which can greatly improve computational cost in evaluating the energies and forces more. However, the immediate challenge is to whether a suitable interatomic potential exist given a chemical system, and moreover, how transferable is it to different compositions and phases.

Recently, there has been a growing effort in the development of machine learning potentials. These deviate from traditional based physics approaches to interatomic potentials, which have historically been inspired from more accurate methods like tight-binding method [1]. In machine learning potentials, one describes the atoms and structure using descriptors (also called features and are used interchangeably here on out) which are typically learned or prescribed. If prescribed, the descriptors can be isolated in terms of structure or composition, or a combination of the two. If needed properties can also be used as part of the descriptor set. compositional, and property characteristics of the material data point. Furthermore, one may choose to fine new representations via unsupervised learning [2].

The subsequent step, once the featurization process is completed, is to determine a suitable machine learning model which can learn the target property or properties given the descriptor inputs. For large data sets Neural Networks have become the preferred choice.

In the case of atomistic simulations the target is prediction of the potential energy surface and corresponding gradients (i.e., forces). Two of the most early ML models to do this were the works of Bartók et al. [3] and Thompson et al. [4], whereby projection onto higher-dimensional basis, such as bispectrum components of local neighbor density, is learned in order to describe the atomic environments. The energy per atom is then determined by these learned features by employing linear regression or non-linear Gaussian process regression. We note that these are just two of the early examples but similar potentials have been developed in earlier, in parallel, or recently by various groups [5, 6, 7, 8].

While these early attempts using ML models were successfully, they may only include limited representations of structural and/or chemical details to learn new features from which could limit transferability. Furthermore, the training process is typically restricted to a limited number of elemental constituents of the target material system. As a consequence, for each chemical system and phases of interest one needs to provide a suitable dataset to learn from (i.e., training). To move beyond such limitations, groups began using graph neural network (GNN) architectures and message passing scheme to represent the atomic structures as nodes and edges [9]. This enabled two distinctions, first being that the nodes and edges corresponding to the atoms and bonds could include features, and secondly the learning could be done over a large structural

and compositional space enabling a generalization<sup>1</sup>. The use of GNNs is efficient in representing structure-composition-property inputs to additional NN layers for predicting potential energy surfaces and gradients and was initially pursued in the CGCNN, MEGNet, and ALIGNN potentials [2, 10, 11]. The differences between the approaches are predominately in atomic and bond features, nearest-neighbor graph, and specific NN architecture.

The training of these early GNN utilized large density functional theory calculation repositories and mostly tuned the learning cost function to ground-state structure and energy. This resulted in mean-absolute-errors and other measures of performance that could be improved upon [12]. More recently there have been significant improvements in both training data used and the GNN architecture that show promise for truly approaching a general interatomic potential suitable for static and dynamic atomistic calculations of multi-components and multi-phases. If successful, identifying and designing new potential SMA materials using GNN interatomic potentials could have tremendous impact on technology.

The primary goal of this work is to provide a qualitative assessment of pre-trained GNN interatomic potentials that are promoted as being transferable across compositions and phases. We specifically focus on the predictions for equations of state, phonon bandstructure, and elastic constants for various phases of NiTi and PtTi using three GNN potentials: M3GNet, CHGNet, and MACE [13, 14, 15]. We note that the Riebesell et al. [12] provides a summarized performance for all of these GNN using the materials project database[16], but does not specifically address SMA and phonon characteristics.

## 2. Computation Methodology

### 2.1. Workflow

To promote reproducible research and align with findable, accessible, interoperable and reusable (FAIR) principles[17], we utilize *show your work!* python workflow[18] and several open source python packages. Instructions for reproducing calculated data, figures, tables, and manuscript are provided in appendix [Appendix A.1](#) and corresponding github repo<sup>2</sup>. We note that in order to achieve the different computing environments required by the interatomic potentials we leverage the ability to specify virtual/containerized python computing environments using *show your work!* package.

### 2.2. Calculation Details

The ground-state structures for the NiTi phases *B2*, *B19*, *B19'*, and *BCO* are generated using the atomic simulation environment (ASE) package [19]. This requires that the unit cell parameters, basis atoms, and spacegroup number be provided. The initial unit cell parameters and basis coordinates for these

---

<sup>1</sup>Typically these are referred to as Universal interatomic potentials or force fields since they in theory generalize well to any chemical system or phase.

<sup>2</sup>[https://github.com/stefanbringquier/SMA\\_Phonons\\_GNNIP](https://github.com/stefanbringquier/SMA_Phonons_GNNIP)

structures have been taken from the materials project [16] and several references [20, 21]. The initial structures for NiTi are shown in fig 1 and are adapted for PtTi as well, given same space group symmetries. The energy and forces on the atoms are determined using the ASE calculator interfaces for EAM, MEAM, M3GNet, CHGNet, and MACE.[22, 23, 24, 25, 13, 14, 15] The EAM and MEAM potential interfaces are achieved through the use of LAMMPS python library [26] and ASE. We have also implemented calculators for potentials by [27], [6], and [2] but are not shown in the main manuscript of this work.

For each combination of potential/model, chemical system, and phase we perform calculations for the structure minimization, equation of state (EOS), phonons, and elastic constants. To determine the finite-temperature phase transitions we utilize an isothermal-isobaric ensemble via molecular dynamics simulations. The thermostating and barostating is done with Nose-Hoover and Parrinello-Rahman dynamics and the ramping down or up of temperature is adjusted in a dynamical manner which entails adjusting the target thermostat temperature every few timesteps based on the ramp-rate. The pressure is kept constant at 1 bar.

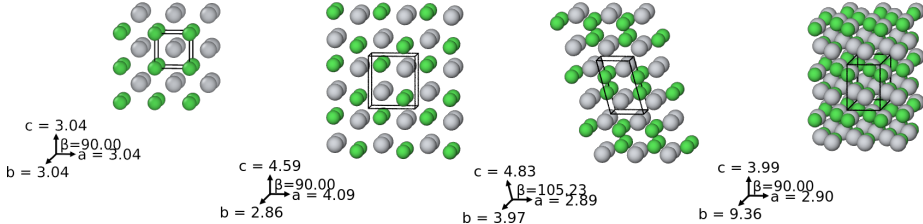


Figure 1: Initial NiTi structures (i.e., unrelaxed) used for (a)  $B2(221)$ , (b)  $B19(11)$ , (c)  $B19'(51)$ , and (d)  $BCO(61)$  with spacegroup numbers are given in the parentheses. The green atoms are Ni and Ti as gray and unit cells are highlighted with parameters shown on axis. For all unit cells the  $\alpha$  and  $\gamma$  angles are  $90.0^\circ$ . For PtTi, (a-b) structures are used with different unit cell parameters and basis coordinates and then optimized accordingly.



Prior to any property calculations or dynamics the structures are optimized using the FIRE[28] local optimizer with the forces converged to  $2 \cdot 10^{-3} \text{ eV}/\text{\AA}$ . We observed that other local optimization routines find the same ground-state structures. To ensure that the unit cell parameters were adjusted along with the atomic coordinates and that the crystal symmetry is not broken, we utilize a constraint and filter during the optimization process.

### 2.2.1. Equation of State

The EOS can be obtained by varying the cell volume and calculating the total system energy without allowing for atomic relaxations. Starting with the obtained ground-state structures the unit cell volume is adjusted by applying an isotropic strain,

$$T = \begin{bmatrix} \epsilon & 0 & 0 \\ 0 & \epsilon & 0 \\ 0 & 0 & \epsilon \end{bmatrix} \quad (1)$$

, to the cell and scaling the fractional atomic coordinates. Here  $\epsilon$  is the fraction strain applied to the unit cell. To ensure that the strain is indeed isotropic we provide a quality check on the symmetry of the distorted structure using the spacegroup package *spglib* [29]. The isotropic strain is applied in compression and tension, from  $-11\%$  to  $11\%$ , which gave a good range to characterize the EOS curves and obtain analytical fits. We fit the EOS using a third order inverse polynomial,

$$E(V) = c_0 + c_1 t + c_2 t^2 + c_3 t^3, \quad \text{where } t = V^{-\frac{1}{3}} \quad (2)$$

, where the coefficients are used to determine equilibrium volume, system energy, and bulk modulus [30] at 0K. In order to compare respective EOS amongst the different phases, we normalize the strained volume of each phase with respect to the obtained minimized ground-state volume.

### 2.2.2. Phonon band structure

Shape memory alloys derive their unique displacive phase transformations from the dynamic instability that occurs during the application of temperature, strain, or stress. The origin of this instability occurs due to softening or symmetry breaking of the phonon modes in the phase. Therefore, improved understanding of the phonon characteristics of the different phases that can occur for a given SMA is particular important.

Phonon calculations are performed using finite-difference method via small displacement (i.e., harmonic approximation) of atoms in a reference cell [31]. In the small displacement method, atoms in the primitive cell are slightly displaced to calculate forces on other atoms, constructing the force constant matrix, which, when used with the dynamical matrix, allows computing phonon frequencies at any q-vector in the Brillouin zone. This requires typically requires the use of a supercell of the original unit cell. In order to ensure convergence of this method, one needs to sweep different supercell sizes and atomic displacements. This process is done for each interatomic potential and structure. The supercells used in this work have a repeat in any one direction ranging from 5–8 and depends on the crystal system. The atomic displacement ranges from  $0.03 - 0.26\text{\AA}$  and was found to strongly depend on interatomic potential and crystal system. Details on the settings are provided in the appendix [Appendix A.3](#).

In order to sample high-symmetry points in the irreducible Brillouin zone (IBZ) for specific structures, we sample from locations specified in the Bilbao crystallographic *KVEC* utility[32], although the ASE structures object does provide a standardized routine for sampling the irreducible Brillouin zone for the specific structures [33]. We predominately focus on high-symmetry points in the IBZ that correspond to the corners and along directions known to exhibit phonon instabilities. The IBZ and points symmetry point locations can be seen in appendix [Appendix A.4](#). The final phonon dispersion diagrams are plot along these points.

To better understand dynamic instability in the various structures, the same isotropic strain in eq. 1 is used and the respective phonon band structure are calculated. These are then plotted to observed the onset or change in stability or instability of phonon different branches.

### 2.2.3. Elastic Constants

Similar to the phonon calculations the elastic constants within the harmonic approximation, can be determined from linear-response of strain-stress calculations. Therefore, the calculation requires the use of crystal symmetry along with atomic displacements to determine respective elastic constant components. We use the *Elastic*[34] python package which provides routines for generating the proper atomic displacement matrix given specific crystal space group. The elastic constants are determined by solving a set of linear equations using singular value decomposition and given calculated strains and stress. The displacements occur with a min and max of 0.5% and a total of 10 points are used.

### 2.2.4. Finite-Temperature Phase Transitions

### 2.3. Physics Based Potentials

The EAM and MEAM potentials were developed to go beyond simpler pair interatomic potentials to treat point and extended defects in metal and alloys systems. The motivation was taken from the physical results of density functional theory and tight-binding methods. The approach was to add to the pair potentials a energy functional which depends on the local atomic environment. These type of interatomic potentials are broadly referred to as EAM or MEAM, with the later included direction dependent interactions (i.e., angular terms).

The functional form using during fitting proceed depends on the complexity of the material system but the total energy is typically written as,

$$E = \sum_{i \neq j}^N V_{ij}(r_{ij}) + \sum_i^N F_i(\rho(r_i)) \quad (3)$$

where  $V_{ij}$  is the pair potential,  $F_i$ , the functional, and  $\rho$  the density function that depends on the environment around  $r_i$ . The MEAM potential extends this by including three-body terms in the  $\rho$  to capture features such as covalent bonding. The EAM and MEAM potentials have been particular successfully in predicting structure and properties of metals and alloys, including defect formation/energies, phase transitions, grain boundary stability/dynamics. One particular advantage of both EAM and MEAM, is their analytical or tabulated forms allow for quick numerical evaluation, with the primary reason being that the energies and forces on a atom are accurately determined within a relatively small interaction volume (i.e., 3-4 Åinteraction cutoff).

For application of EAM to shape memory alloys, and in particular NiTi, Mutter and Nielaba [22] initially devised an Finnis-Sinclair style EAM potential to capture the structural phase transitions between  $B19'$  and  $B2$  phases. It was latter shown by [23] that some adjustments to the EAM parameters

were needed to properly capture the finite-temperature displacement dynamics for the martensitic transition [35]. More recently Ko et al. [24] developed a second nearest neighbor(2NN) MEAM parameterization of NiTi that demonstrated very good predictive performance and improvements over earlier potentials.

#### 2.4. Graph Neural Network Potentials

The use of ML potentials for SMA has been demonstrated by Tang et al. [36]. In their work, they utilized the DeePMD-Kit[6] neural network framework to parameterize a descriptor matrix from atomic configurations that preserves permutations and symmetries. The descriptors are then feed into a multilayer perceptron to calculate energies and forces. The neural network interatomic potential demonstrated good accuracy of ground-state properties with respect to DFT results and showed agreement with experiments regarding temperature, stress, and defect induced martensitic transformation. The ground-state predictions for  $B2$ ,  $B19'$ ,  $B19$ , and  $BCO$ <sup>3</sup> in Tang et al. [36] showed good agreement. However, we note that deviation from Ni-Ti 1:1 stoichiometry or addition of a third species was not investigated nor the inclusion of additional alloying species was explored.

The pre-trained GNN interatomic potentials explored in this work have been parameterized over a large fraction of the interatomic potential ( $> 80$  elements) and therefore are not restricted to specific chemistries or stoichiometries. The training data also includes various phases for a given chemical system which permits great flexibility, although broad transferability still requires verification. This allows for investigation of both non-stoichiometric and multi-species SMA which previous physics and ML potentials were not developed for. We do note that fine-tuning, the process of adjusting GNN weights and biases using additional training data, can be performed with the GNNs studied in this work. However, this is out of the scope for this manuscript, given resources and time needed to generate such training data for SMAs.

The M3GNet is a GNN that utilizes a 3-body bond-update procedure to more accurately capture bond-order environment changes. The M3GNet has been implemented in the MatGL framework and we utilize the `M3GNet-MP-2021.2.8-PES` pretrained model.

For CHGNet, we have used the v0.3 series pretrained model.

### 3. Results

In fig. 2 the density of the structures for different potentials is shown. We observe that in general the densities and lattice parameters are within agreement with previously reported values. The optimized lattice parameters as well as basis atoms for all structures and models are provided in appendix [Appendix A.2](#).

---

<sup>3</sup>Referred to as  $B33$  prototype in Tang et al. [36]

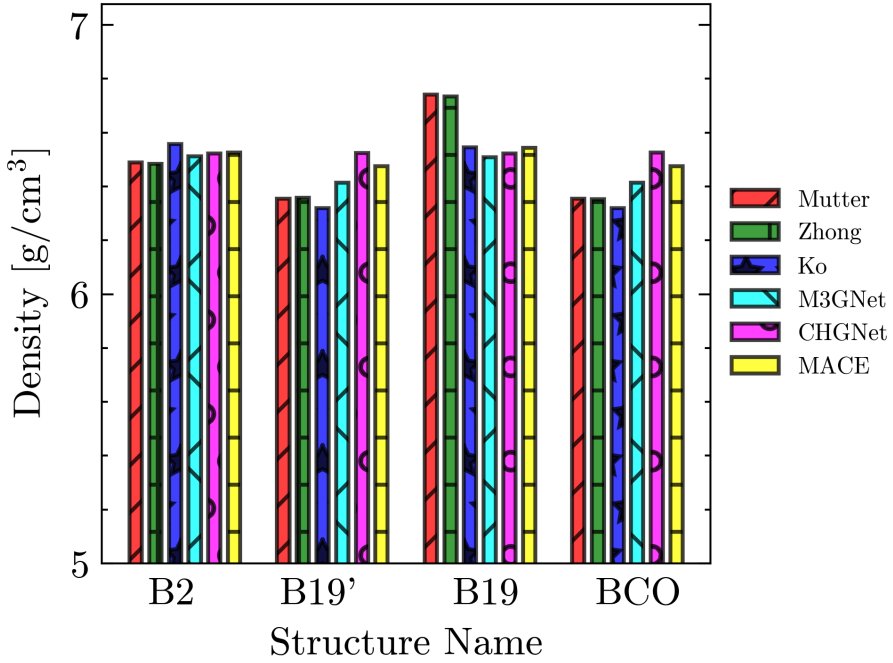


Figure 2: Equilibrium Density for NiTi structures with different models.

To asses the relative phase stability for a given composition is to compare the cohesive energy, which is defined as,

$$E_c = \frac{E_{\text{bulk}} - \sum_i^N n_i E_{\text{atom}_i}}{N} \quad (4)$$

With  $E_{\text{bulk}}$  the total energy of the system,  $\sum_i^N n_i E_{\text{atom}_i}$  is the sum over isolated atom energies for  $n_i$  species, and  $N$  the number of atoms in bulk reference. Classical interatomic potentials are offset with respect to the isolated atom energies, so these terms are zero and neglected, giving  $E_c = \frac{E_{\text{bulk}}}{N}$ . In fig. 3 the bar chart for different phases and interatomic potentials models are show. We compare these to dervived experimental values for  $B2$ [37] and the value from The Materials Project (MP) entry MP-571 which corresponds to the  $B2$  phase [38]. In the figure we see that the EAM and MEAM potentials show significantly lower cohesive energy compared to the GNN potentials and are in better agreement with the experimental value. Previous studies using the EAM and MEAM potentials have been shown to reproduce previous experimental and DFT data [20, 24] such as cohesive energy. The GNNs predict a more strongly bound and stable  $B2$  structure but all are consistent with the entry for The MP and calculation details can be found in ref. [38]. This consistency is reasonable considering all pretrained GNN models used in this work have been developed with MP data.

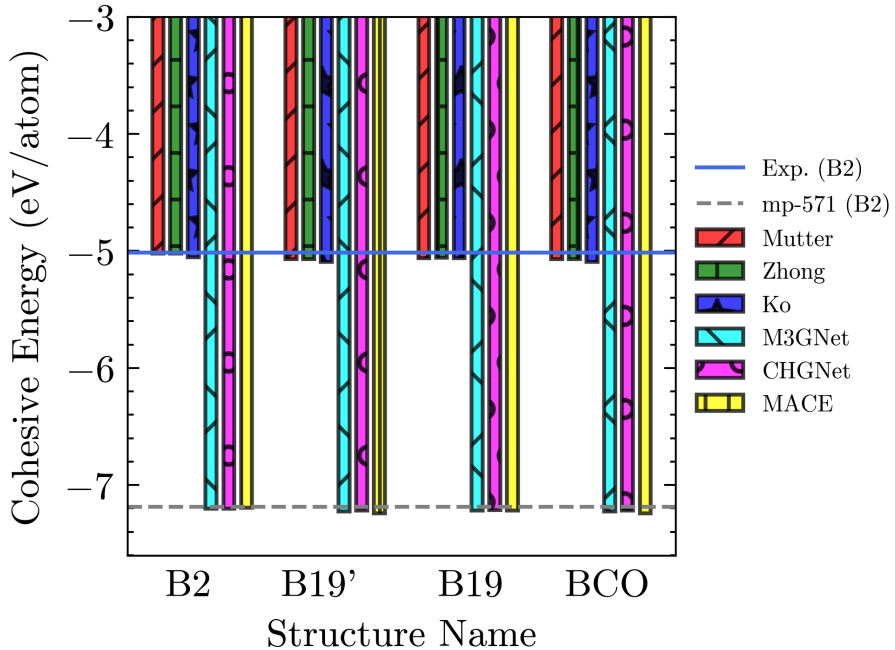


Figure 3: Comparison of predicted NiTi cohesive energy for respective ground-state structure and model. The experimental data point has been extracted from ref. [37] and the Materials Project entry for the NiTi *B2* structure [38] has also been included.



For the PtTi system we only consider the *B2* and *B19'* structures. The MEAM potential shows a lower cohesive energy than all three GNN. Interestingly the difference between the MEAM and GNN is roughly the same order,  $\approx 2.1$  eV, which maybe appears to be related to the MP dataset. To our knowledge most the pretrained GNN models are using the MP dataset which defaults to DFT calculation results that employ the meta-GGA R2SCAN functional. This could be the reason for the difference as most EAM and MEAM potentials are either parameterized from experimental or DFT data using the PBE functional[22, 24].

### 3.1. NiTi: Equation of States

The EOS curves for the NiTi structures *B2*, *B19*, *B19'*, *BCO* for the different potentials studied in this work are shown in fig. 5. The two EAM potentials, show that at 0 strain ( $V/V_o = 1.0$ ) both the *B19P* and *B33* phases are stable. I believe this is the first reporting of the *B33* phase for these two fittings of the EAM potential for NiTi. Its important to note that these potentials have been developed to capture the displacive phase transformation between *B19P* to *B2*. This is shown in fig. 5(a,b) with the stability indicated upon compressive isotropic strain. A minimum appears around  $\approx 0.9$ . At tensile isotropic strains

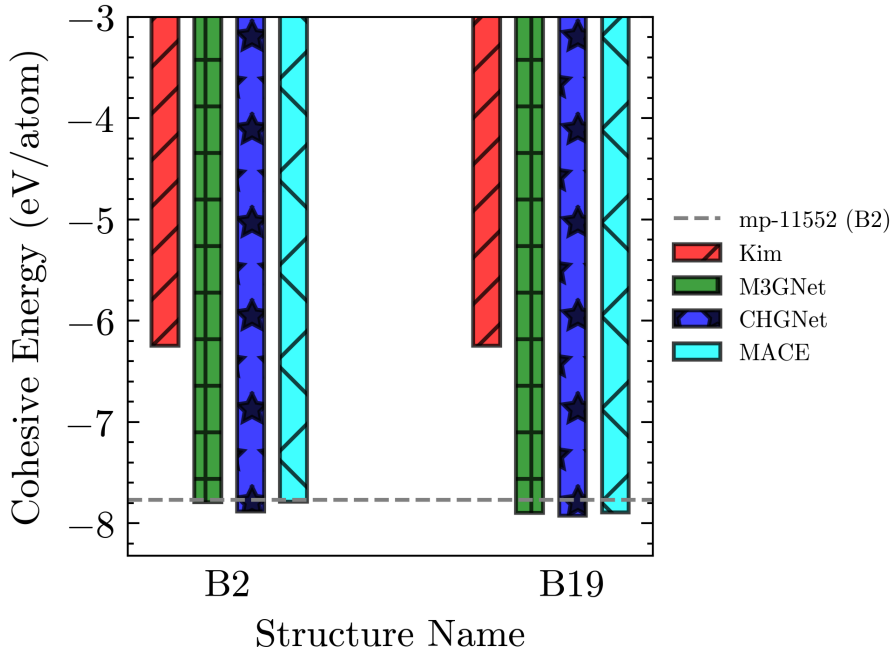


Figure 4: Comparison of predicted PtTi cohesive energy for respective ground-state structure and model.



the  $B19P$  phase is stable up till around 1.18 where the  $Pbcm$  phase shows stability. An interesting note is that these two fittings of the EAM potential show a double well curve for the  $B2$  phase.

In the UIP-GNN potentials M3GNet, CHGNet, and MACE, the equation of states shown in fig. 5(c-e) look fairly different from thos in fig. 5(a,b). For the M3GNet, at no strain, the  $B33$  appears to be the predicted stable phase and the  $B2$  phase becomes stable around 0.9 (see fig. 5(c)). The stability for  $B19$  and  $B19P$  exit, in trade-off, between approximately 1.025 and 1.1 tensile isotropic strain. Interestingly beyond a strain of 1.1 the  $Pbcm$  is dominate. The double-well curve shown for the EAM potentials is not present for the  $B2$ -phase. The CHGNet potential results shown in fig. 5(d) are similar to the M3GNet, but the stability window of the  $B2$  occurs at a lower compressive isotropic strain.

The MACE potential shown in fig. 5(e) has a very different set of EOS curves compared to the M3GNet and CHGNet. Here many of the phases exhibit a stability window, except the  $B33$  phase, which was stable in M3GNet and CHGNet. Interestingly, the  $B19$  phase, not the  $B19P$  phase is shown to be the stable zero strain phase. One unique perspective of the the UIP-GNN models is that they provide a different displacive phase transformation pathway then that shown by the EAM potentials. However, this does not include the meta-stable R-phase or other potential meta-stable phases which can also offer such

transformation mechanisms.

Finally, the ALIGNN potential EOS was generated, but a few issues arose during the calculations. The most prominent was the difficulty in convergence of the structural optimization to the specified tolerance (see 2). Secondly the calculated cohesive energies differs from the UIP-GNN by a factor  $\approx 2$  and by 1 eV for the EAM potentials. The *B19P* phase is the stable at zero strain and for a considerable portion of the compressive, but all of the tensile. At compressive strain beyond  $\approx 0.94$  the *B2* phase is stable.

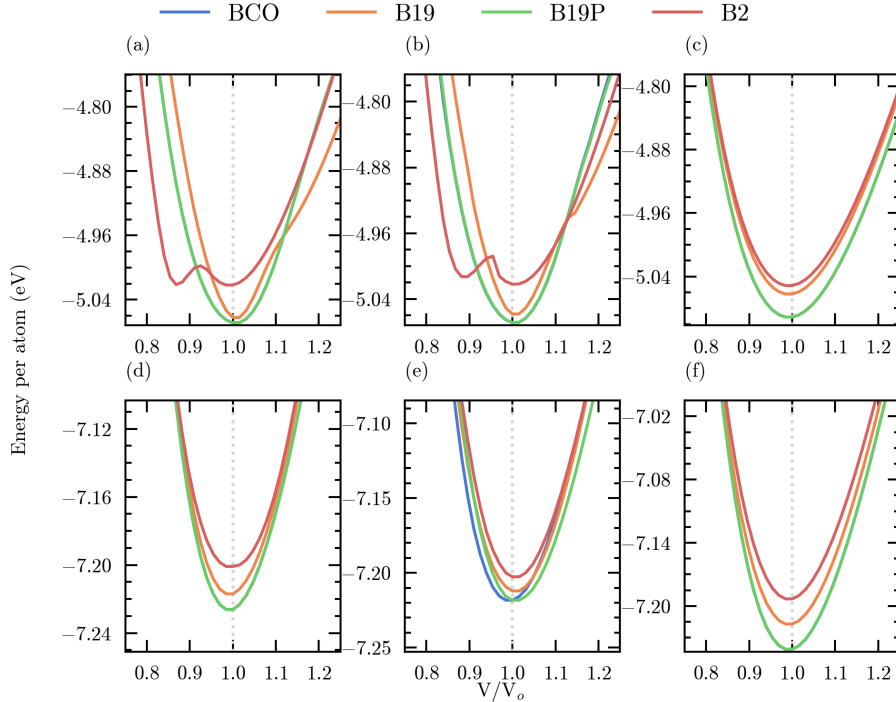


Figure 5: The equation of state curves for different NiTi structures for (a) Mutter (EAM) (b) Zhong (EAM) (c) Ko (2NN-MEAM) (d) M3GNet (e) CHGNet (f) MACE interatomic potentials. The x-axis is the ratio of the isotropic strained unit cell volume,  $V$ , with respect to the ground-state unit cell volume,  $V_o$ .



### 3.2. NiTi: Phonon Instability

In the context of NiTi alloys, phonon instabilities play a crucial role in understanding the phase stability and transformations. The phonon band structures for *B2* phase, as shown in Fig. 6, reveal that the Mutter EAM potential predicts no dynamic instability at 0K. In contrast the Zhong EAM potential predicts onset of dynamic instability. In contrast, the Ko and MACE models exhibit phonon softening along the  $\Gamma - M$  direction, aligning well with DFT

results [39]. The M3GNet and CHGNet models predict also predict mode instability but qualitatively differs significantly. This suggests that Ko and MACE models more accurately capture the intrinsic instability of the  $B2$  phase, crucial for predicting the martensitic transformation to  $B19'$  or  $BCO$  phases.

For the  $B19$  phase, Fig. 7, the phonon band structures indicate instability in the  $\Gamma - Y/B$  directions, consistent with DFT predictions. The Ko, CHGNet, and MACE models display similar trends, albeit with slight discrepancies. Furthermore, the  $B19'$  and  $BCO$  phases, illustrated in Fig. ?? and Fig. 9, respectively, highlight the stability predicted by DFT. Notably, only the Mutter, Zhong, and Ko models predict no mode instability for  $B19'$  and  $BCO$ , while the others indicate potential mode instability. This reinforces the necessity here for fine-tuned GNN potentials that can accurately capture the complex phonon dynamics and phase stability in NiTi alloys.

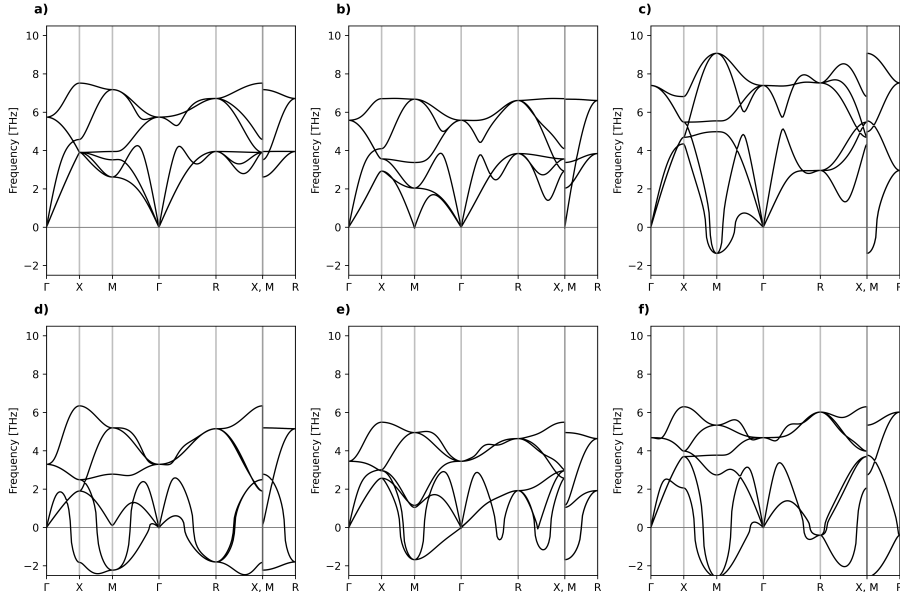


Figure 6: Ground-state, no isotropic strain, Phonon bandstructure of  $B2$  phase for all models. The Mutter (a) and Zhong (b) EAM potentials differ in that Mutter predicts no dynamic instability of the  $B2$  phase at 0K. The results for Ko (c), M3GNet (d), CHGNet (e), and MACE (f) all display the instability from  $\Gamma - M$ . The Ko (c) and MACE (f) models appear to agree best with DFT results [39].



### 3.2.1. Mode Grunéisen Parameter

The  $B2$  phase of NiTi exhibits notable phonon instabilities, particularly at the  $M$  point in the Brillouin zone. These instabilities are characterized by imaginary modes, represented as negative phonon frequencies, indicating a dynamical instability in this crystal structure. The  $M$  point, located at the edge of the Brillouin zone, corresponds to a wave vector of  $[\frac{1}{2}, \frac{1}{2}, 0]$  in units of the reciprocal

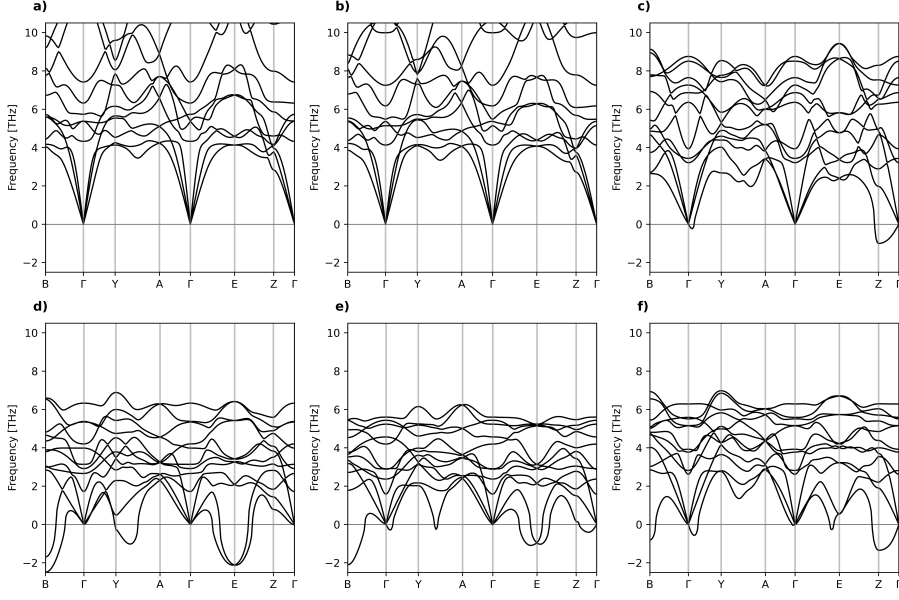


Figure 7: Ground-state phonon bandstructure of B19 phase for all models. Plots (a-f) follow same ordering as in fig. 6. The DFT results in ref. [39] indicate instability in  $\Gamma$ -Y/B directions. In (c,e-f) the results are similar to the DFT but slight differ.

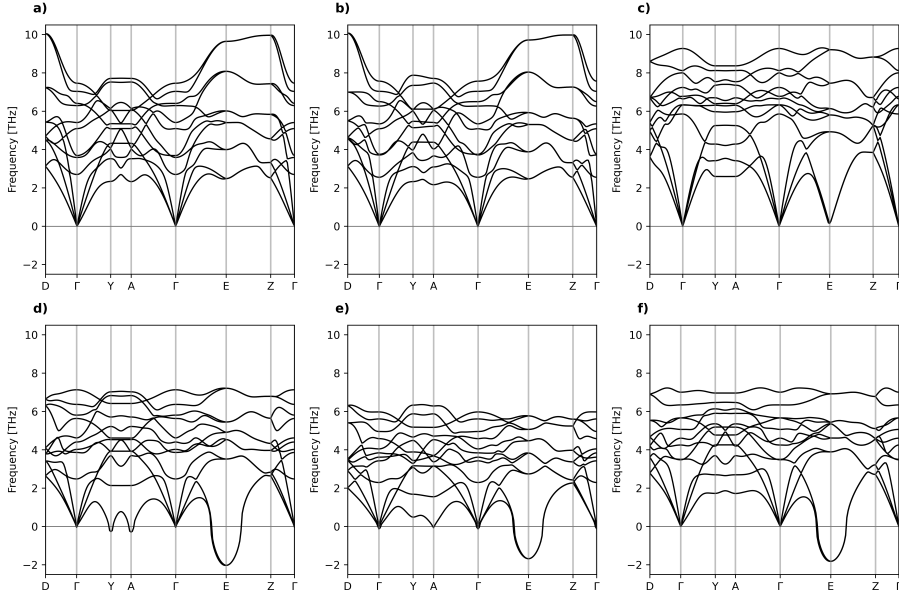


Figure 8: Ground-state phonon bandstructure of  $B19'$  phase for all models. Plots (a-f) follow same ordering as in fig. 6. As indicated by DFT this should be a potential stable structure however only (a-c) show no mode instability.

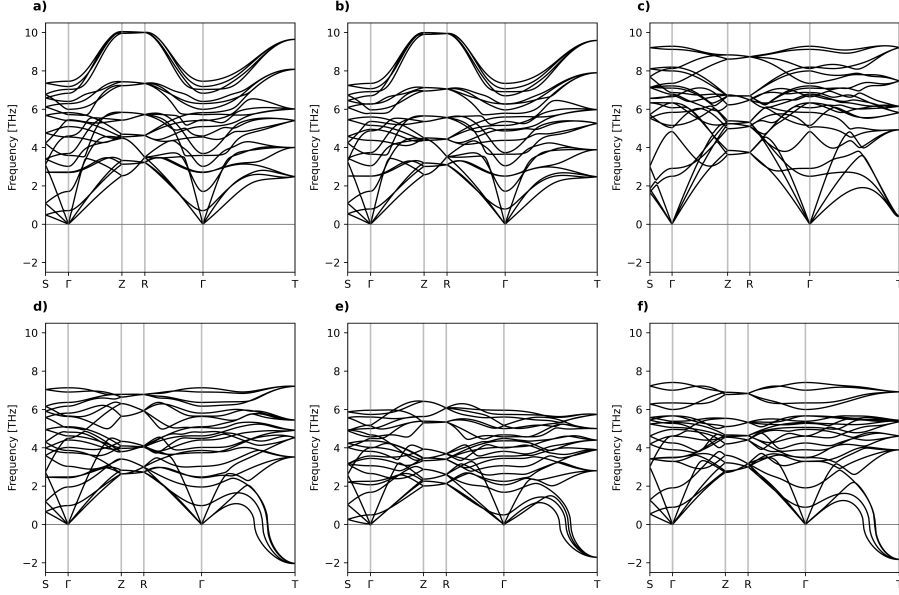


Figure 9: round-state phonon bandstructure of BCO phase for all models. Plots (a-f) follow same ordering as in fig. 6. As indicated by DFT this should be a potential stable structure however only (a-c) show no mode instability.



lattice vectors. The phonon dispersion curves for NiTi in the B2 phase reveal a softening of the acoustic modes at the  $M$  point, suggesting a propensity for a structural phase transition.

The mode Gruneisen parameter,  $\gamma$ , plays a pivotal role in understanding the stabilization of the NiTi B2 phase under external strain, particularly in the context of phonon instabilities at the  $M$  point. The mode Gruneisen parameter is defined as,

$$\gamma = -\frac{V}{\omega} \left( \frac{\partial \omega}{\partial V} \right) \quad (5)$$

where  $V$  is the volume, usually taken at equilibrium, and  $\omega$  is the phonon frequency. For the  $B2$  phase of NiTi, the negative phonon frequencies at the  $M$  point indicate an instability that can be modulated by applying strain. The strain perturbs the lattice volume, thereby altering the phonon frequencies. The effect of this strain can be quantitatively assessed using the mode Grüneisen parameter, which describes how the phonon frequencies change with volume. A positive  $\gamma$  suggests that the phonon frequency increases as the volume decreases under strain, potentially stabilizing the lattice. In the case of NiTi, applying compressive strain may increase the frequencies of the soft modes at the  $M$  point, thus stabilizing the  $B2$  phase and delaying or suppressing the martensitic transformation. This interplay between strain and phonon behavior, quantified

by  $\gamma$ , is crucial in tailoring the mechanical properties of shape memory and superelastic materials.

In fig. 10 the Grüneisen parameter for  $M$ -mode in  $B2$  is shown for different interatomic potentials for NiTi. The instable modes (i.e., negative eigenfrequencies) for the MEAM, M3GNet, and MACE potentials have Grüneisen parameter which are negative. The negative values suggest that compressive isotropic strains will provide stabilizing force against displacive phase transformation. At higher frequencies the Grüneisen parameter is positive, indicating this modes experience a decrease in frequency with respect to volume increase. The optical modes are less sensitive as indicated by smaller values.

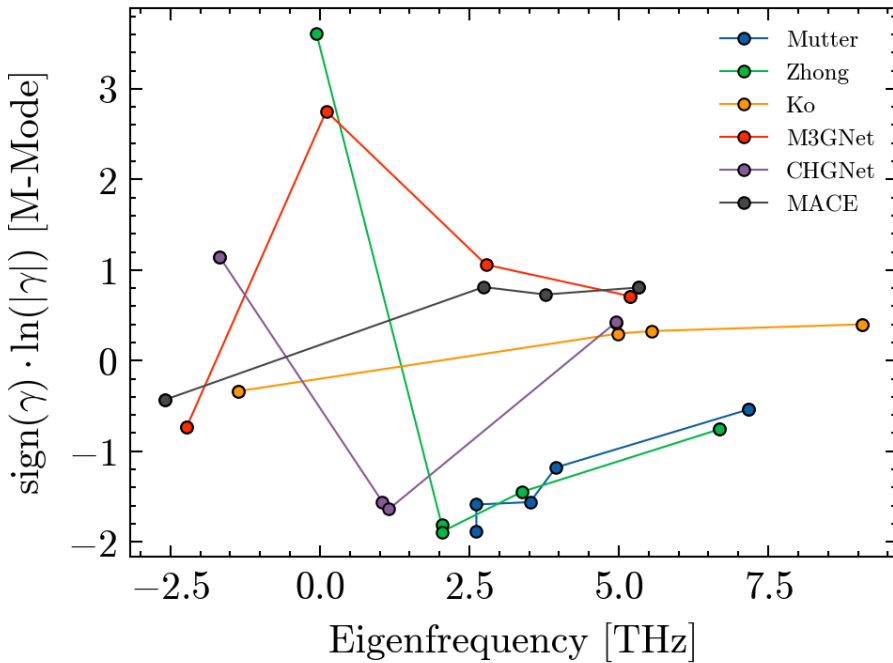


Figure 10: The sign-log of the  $M$ -mode Grüneisen parameter,  $\gamma$ , as a function of eigenfrequency for different interatomic potentials.

The Mutter EAM potential shows negative Grüneisen parameters for all eigenfrequencies indicating compressive forces increase frequencies, however, none of the  $M$ -point modes have negative eigenfrequencies.

In contrast the the MEAM, M3GNet, and MACE potentials, the Zhong EAM and CHGNet potentials show positive Grüneisen parameters for negative eigenfrequencies, suggesting that isotropic tensile strain acts to stabilize the mode.

To better corroborate the results in fig. 10, the phonon band structure as a result of isotropic strain applied in compression and tension are shown in fig

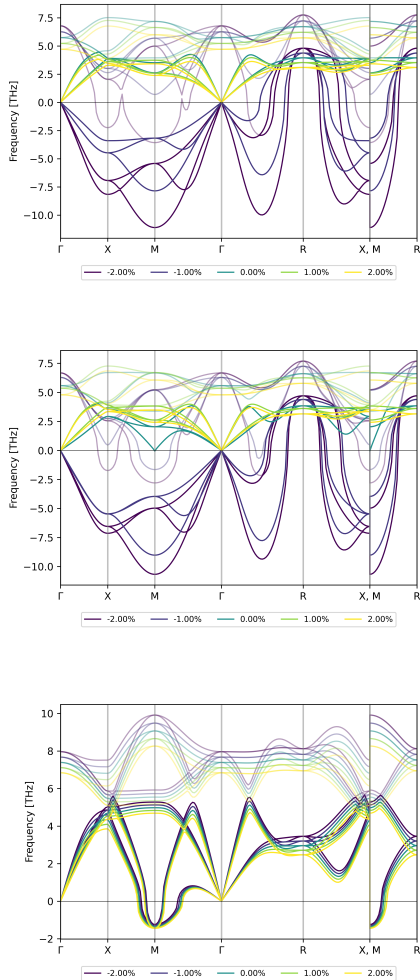


Figure 11: Phonon dispersion of B2 structure for the (top) EAM Mutter, (middle) EAM Zhong, and (bottom) 2NN-MEAM Ko potentials at different isotropic strains. The optical branches have been made more transparent to emphasize the behavior in the TA<sub>1</sub> and TA<sub>2</sub> branches. The color indicates direction from compressive to tensile strain. Note that the strain percent shown is with respect to isotropic changes (i.e., volume).



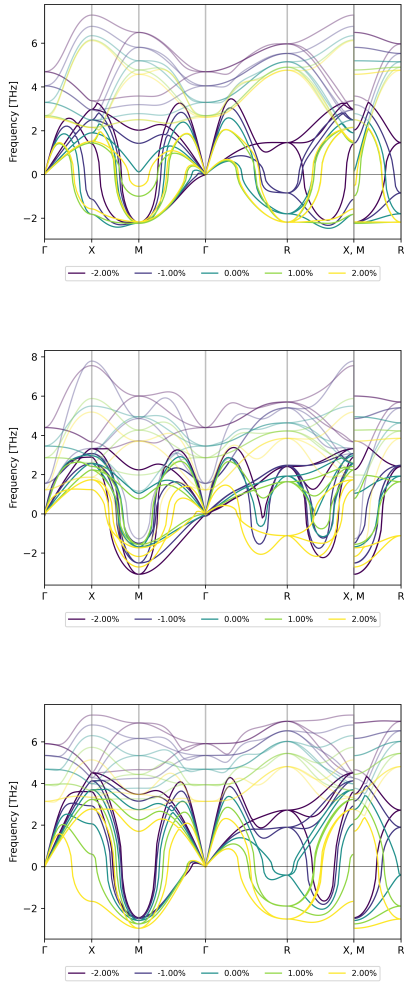


Figure 12: Phonon dispersion of B2 structure for the (top) M3GNet, (middle) CHGNet, and (bottom) MACE potentials for different isotropic strains. Similar transparency is used as done in 11.



### *3.2.2. Elastic Constants*

Table 1: Elastic constants for NiTi.

Structure (#)	Properties													
	Model	C <sub>11</sub>	C <sub>22</sub>	C <sub>33</sub>	C <sub>12</sub>	C <sub>13</sub>	C <sub>23</sub>	C <sub>44</sub>	C <sub>55</sub>	C <sub>66</sub>	C <sub>16</sub>	C <sub>26</sub>	C <sub>36</sub>	C <sub>45</sub>
B2 (221)	Mutter	205	-	-	136	-	-	48	-	-	-	-	-	-
	Zhong	186	-	-	115	-	-	44	-	-	-	-	-	-
	Ko	143	-	-	128	-	-	80	-	-	-	-	-	-
	M3GNet	121	-	-	112	-	-	13	-	-	-	-	-	-
	CHGNet	129	-	-	152	-	-	23	-	-	-	-	-	-
	MACE	161	-	-	152	-	-	48	-	-	-	-	-	-
B19P (11)	Model	C <sub>11</sub>	C <sub>22</sub>	C <sub>33</sub>	C <sub>12</sub>	C <sub>13</sub>	C <sub>23</sub>	C <sub>44</sub>	C <sub>55</sub>	C <sub>66</sub>	C <sub>16</sub>	C <sub>26</sub>	C <sub>36</sub>	C <sub>45</sub>
	Mutter	187	441	240	147	108	127	34	26	63	-0	-1	-0	0
	Zhong	155	790	243	142	108	168	38	33	56	6	10	-0	22
	Ko	164	203	226	123	77	102	103	100	125	-0	0	0	0
	M3GNet	154	206	207	127	104	128	39	23	46	-0	-0	-0	0
	CHGNet	117	185	197	95	92	125	30	11	22	-1	-1	0	1
B19 (51)	Model	C <sub>11</sub>	C <sub>22</sub>	C <sub>33</sub>	C <sub>12</sub>	C <sub>13</sub>	C <sub>23</sub>	C <sub>44</sub>	C <sub>55</sub>	C <sub>66</sub>	C <sub>16</sub>	C <sub>26</sub>	C <sub>36</sub>	C <sub>45</sub>
	Mutter	1306	665	313	388	249	310	214	139	266	-	-	-	-
	Zhong	950	622	275	356	165	264	147	105	199	-	-	-	-
	Ko	222	183	220	107	83	104	78	37	90	-	-	-	-
	M3GNet	167	142	183	120	126	130	27	19	14	-	-	-	-
	CHGNet	208	188	183	138	112	129	35	23	33	-	-	-	-
	MACE	224	174	222	139	128	137	40	31	44	-	-	-	-

Table 1: Elastic constants for NiTi. (Continued)

Structure	Properties	Model	C <sub>11</sub>	C <sub>22</sub>	C <sub>33</sub>	C <sub>12</sub>	C <sub>13</sub>	C <sub>23</sub>	C <sub>44</sub>	C <sub>55</sub>	C <sub>66</sub>	C <sub>16</sub>	C <sub>26</sub>	C <sub>36</sub>	C <sub>45</sub>
		Mutter	187	240	441	108	147	127	34	63	26	-	-	-	-
BCO (63)	Zhong	195	191	712	87	138	83	35	57	21	-	-	-	-	-
	Ko	164	226	203	77	123	102	103	125	100	-	-	-	-	-
	M3GNet	154	207	206	104	127	128	39	46	23	-	-	-	-	-
	CHGNet	126	199	201	101	105	136	32	23	16	-	-	-	-	-
	MACE	167	239	232	132	147	144	51	61	29	-	-	-	-	-



### 3.3. PtTi: Equation of States

## 4. Conclusion

This work provides a first step in the assessment of pre-trained universal GNN interatomic potentials on ability to model SMA materials. In addition, the dynamic stability of these SMA is crucially evaluated through phonon band structures to understand the suitability in observing the onset of displacive phase transformations via the softening modes. In the case of NiTi we find that all the GNN potentials predict either the Monoclinic or BCO phases as stable over the B2 structure. However, not all agree with relatively recent works [20, 39] that indicate *BCO* or *B33* phase is the ground-state structure.

## References

- [1] M. Finnis, Interatomic Forces in Condensed Matter, Oxford Series on Materials Modelling, Oxford University Press, Oxford, New York, 2010.
- [2] K. Choudhary, B. DeCost, Atomistic Line Graph Neural Network for improved materials property predictions, *npj Computational Materials* 7 (2021) 1–8. doi:[10.1038/s41524-021-00650-1](https://doi.org/10.1038/s41524-021-00650-1).
- [3] A. P. Bartók, M. C. Payne, R. Kondor, G. Csányi, Gaussian Approximation Potentials: The Accuracy of Quantum Mechanics, without the Electrons, *Physical Review Letters* 104 (2010) 136403. doi:[10.1103/PhysRevLett.104.136403](https://doi.org/10.1103/PhysRevLett.104.136403).
- [4] A. P. Thompson, L. P. Swiler, C. R. Trott, S. M. Foiles, G. J. Tucker, Spectral neighbor analysis method for automated generation of quantum-accurate interatomic potentials, *Journal of Computational Physics* 285 (2015) 316–330. doi:[10.1016/j.jcp.2014.12.018](https://doi.org/10.1016/j.jcp.2014.12.018).
- [5] J. Behler, M. Parrinello, Generalized Neural-Network Representation of High-Dimensional Potential-Energy Surfaces, *Physical Review Letters* 98 (2007) 146401. doi:[10.1103/PhysRevLett.98.146401](https://doi.org/10.1103/PhysRevLett.98.146401).
- [6] H. Wang, L. Zhang, J. Han, W. E, DeePMD-kit: A deep learning package for many-body potential energy representation and molecular dynamics, *Computer Physics Communications* 228 (2018) 178–184. doi:[10.1016/j.cpc.2018.03.016](https://doi.org/10.1016/j.cpc.2018.03.016).
- [7] V. L. Deringer, M. A. Caro, G. Csányi, Machine Learning Interatomic Potentials as Emerging Tools for Materials Science, *Advanced Materials* 31 (2019) 1902765. doi:[10.1002/adma.201902765](https://doi.org/10.1002/adma.201902765).

- [8] K. Lee, D. Yoo, W. Jeong, S. Han, SIMPLE-NN: An efficient package for training and executing neural-network interatomic potentials, Computer Physics Communications 242 (2019) 95–103. doi:[10.1016/j.cpc.2019.04.014](https://doi.org/10.1016/j.cpc.2019.04.014).
- [9] P. Reiser, M. Neubert, A. Eberhard, L. Torresi, C. Zhou, C. Shao, H. Metni, C. van Hoesel, H. Schopmans, T. Sommer, P. Friederich, Graph neural networks for materials science and chemistry, Communications Materials 3 (2022) 1–18. doi:[10.1038/s43246-022-00315-6](https://doi.org/10.1038/s43246-022-00315-6).
- [10] C. Chen, W. Ye, Y. Zuo, C. Zheng, S. P. Ong, Graph Networks as a Universal Machine Learning Framework for Molecules and Crystals, Chemistry of Materials 31 (2019) 3564–3572. doi:[10.1021/acs.chemmater.9b01294](https://doi.org/10.1021/acs.chemmater.9b01294).
- [11] T. Xie, J. C. Grossman, Crystal Graph Convolutional Neural Networks for an Accurate and Interpretable Prediction of Material Properties, Physical Review Letters 120 (2018) 145301. doi:[10.1103/PhysRevLett.120.145301](https://doi.org/10.1103/PhysRevLett.120.145301). arXiv:[1710.10324](https://arxiv.org/abs/1710.10324).
- [12] J. Riebesell, R. E. A. Goodall, A. Jain, P. Benner, K. A. Persson, A. A. Lee, Matbench Discovery – An evaluation framework for machine learning crystal stability prediction, 2023. doi:[10.48550/arXiv.2308.14920](https://doi.org/10.48550/arXiv.2308.14920). arXiv:[2308.14920](https://arxiv.org/abs/2308.14920).
- [13] C. Chen, S. P. Ong, A universal graph deep learning interatomic potential for the periodic table, Nature Computational Science 2 (2022) 718–728. doi:[10.1038/s43588-022-00349-3](https://doi.org/10.1038/s43588-022-00349-3).
- [14] B. Deng, P. Zhong, K. Jun, J. Riebesell, K. Han, C. J. Bartel, G. Ceder, CHGNet as a pretrained universal neural network potential for charge-informed atomistic modelling, Nature Machine Intelligence 5 (2023) 1031–1041. doi:[10.1038/s42256-023-00716-3](https://doi.org/10.1038/s42256-023-00716-3).
- [15] I. Batatia, D. P. Kovacs, G. N. C. Simm, C. Ortner, G. Csanyi, MACE: Higher Order Equivariant Message Passing Neural Networks for Fast and Accurate Force Fields, in: Advances in Neural Information Processing Systems, 2022.
- [16] A. Jain, S. P. Ong, G. Hautier, W. Chen, W. D. Richards, S. Dacek, S. Cholia, D. Gunter, D. Skinner, G. Ceder, K. A. Persson, Commentary: The Materials Project: A materials genome approach to accelerating materials innovation, APL Materials 1 (2013) 011002. doi:[10.1063/1.4812323](https://doi.org/10.1063/1.4812323).
- [17] A. Walsh, Open computational materials science, Nature Materials (2024) 1–2. doi:[10.1038/s41563-023-01699-7](https://doi.org/10.1038/s41563-023-01699-7).
- [18] R. Luger, M. Bedell, D. Foreman-Mackey, I. J. M. Crossfield, L. L. Zhao, D. W. Hogg, Mapping stellar surfaces III: An efficient, scalable, and open-source doppler imaging model, arXiv e-prints (2021).

- [19] A. H. Larsen, J. J. Mortensen, J. Blomqvist, I. E. Castelli, R. Christensen, M. Dułak, J. Friis, M. N. Groves, B. Hammer, C. Hargus, E. D. Hermes, P. C. Jennings, P. B. Jensen, J. Kermode, J. R. Kitchin, E. L. Kolsbørg, J. Kubal, K. Kaasbjerg, S. Lysgaard, J. B. Maronsson, T. Maxson, T. Olsen, L. Pastewka, A. Peterson, C. Rostgaard, J. Schiøtz, O. Schütt, M. Strange, K. S. Thygesen, T. Vegge, L. Vilhelmsen, M. Walter, Z. Zeng, K. W. Jacobsen, The atomic simulation environment—a Python library for working with atoms, *Journal of Physics: Condensed Matter* 29 (2017) 273002. doi:[10.1088/1361-648X/aa680e](https://doi.org/10.1088/1361-648X/aa680e).
- [20] J. B. Haskins, A. E. Thompson, J. W. Lawson, Ab initio simulations of phase stability and martensitic transitions in NiTi, *Physical Review B* 94 (2016) 214110. doi:[10.1103/PhysRevB.94.214110](https://doi.org/10.1103/PhysRevB.94.214110).
- [21] S. Kadkhodaei, A. van de Walle, First-principles calculations of thermal properties of the mechanically unstable phases of the PtTi and NiTi shape memory alloys, *Acta Materialia* 147 (2018) 296–303. doi:[10.1016/j.actamat.2018.01.025](https://doi.org/10.1016/j.actamat.2018.01.025).
- [22] D. Mutter, P. Nielaba, Simulation of structural phase transitions in NiTi, *Physical Review B* 82 (2010) 224201. doi:[10.1103/PhysRevB.82.224201](https://doi.org/10.1103/PhysRevB.82.224201).
- [23] Y. Zhong, K. Gall, T. Zhu, Atomistic study of nanotwins in NiTi shape memory alloys, *Journal of Applied Physics* 110 (2011) 033532. doi:[10.1063/1.3621429](https://doi.org/10.1063/1.3621429).
- [24] W.-S. Ko, B. Grabowski, J. Neugebauer, Development and application of a Ni-Ti interatomic potential with high predictive accuracy of the martensitic phase transition, *Physical Review B* 92 (2015) 134107. doi:[10.1103/PhysRevB.92.134107](https://doi.org/10.1103/PhysRevB.92.134107).
- [25] J.-S. Kim, D. Seol, J. Ji, H.-S. Jang, Y. Kim, B.-J. Lee, Second nearest-neighbor modified embedded-atom method interatomic potentials for the Pt-M (M = Al, Co, Cu, Mo, Ni, Ti, V) binary systems, *Calphad* 59 (2017) 131–141. doi:[10.1016/j.calphad.2017.09.005](https://doi.org/10.1016/j.calphad.2017.09.005).
- [26] A. P. Thompson, H. M. Aktulga, R. Berger, D. S. Bolintineanu, W. M. Brown, P. S. Crozier, P. J. in 't Veld, A. Kohlmeyer, S. G. Moore, T. D. Nguyen, R. Shan, M. J. Stevens, J. Tranchida, C. Trott, S. J. Plimpton, LAMMPS - a flexible simulation tool for particle-based materials modeling at the atomic, meso, and continuum scales, *Computer Physics Communications* 271 (2022). doi:[10.1016/j.cpc.2021.108171](https://doi.org/10.1016/j.cpc.2021.108171).
- [27] S. Kavousi, B. R. Novak, M. I. Baskes, M. A. Zaeem, D. Moldovan, Modified embedded-atom method potential for high-temperature crystal-melt properties of Ti–Ni alloys and its application to phase field simulation of solidification, *Modelling and Simulation in Materials Science and Engineering* 28 (2019) 015006. doi:[10.1088/1361-651X/ab580c](https://doi.org/10.1088/1361-651X/ab580c).

- [28] E. Bitzek, P. Koskinen, F. Gähler, M. Moseler, P. Gumbsch, Structural Relaxation Made Simple, *Physical Review Letters* 97 (2006) 170201. doi:[10.1103/PhysRevLett.97.170201](https://doi.org/10.1103/PhysRevLett.97.170201).
- [29] A. Togo, I. Tanaka, Spglib: A software library for crystal symmetry search, 2018. [arXiv:1808.01590](https://arxiv.org/abs/1808.01590).
- [30] A. B. Alchagirov, J. P. Perdew, J. C. Boettger, R. C. Albers, C. Fiolhais, Reply to “Comment on ‘Energy and pressure versus volume: Equations of state motivated by the stabilized jellium model’ ”, *Physical Review B* 67 (2003) 026103. doi:[10.1103/PhysRevB.67.026103](https://doi.org/10.1103/PhysRevB.67.026103).
- [31] D. Alfe, PHON: A program to calculate phonons using the small displacement method, *Computer Physics Communications* 180 (2009) 2622–2633. doi:[10.1016/j.cpc.2009.03.010](https://doi.org/10.1016/j.cpc.2009.03.010).
- [32] M. I. Aroyo, D. Orobengoa, G. de la Flor, E. S. Tasçi, J. M. Perez-Mato, H. Wondratschek, Brillouin-zone database on the *bilbao crystallographic server*, *Acta Crystallographica Section A* 70 (2014) 126–137. doi:[10.1107/S205327331303091X](https://doi.org/10.1107/S205327331303091X).
- [33] W. Setyawan, S. Curtarolo, High-throughput electronic band structure calculations: Challenges and tools, *Computational Materials Science* 49 (2010) 299–312. doi:[10.1016/j.commatsci.2010.05.010](https://doi.org/10.1016/j.commatsci.2010.05.010).
- [34] P. T. Jochym, C. Badger, Jochym/Elastic: Maintenance release, Zenodo, 2018. doi:[10.5281/zenodo.1254570](https://doi.org/10.5281/zenodo.1254570).
- [35] S. Gur, V. R. Manga, S. Bringuer, K. Muralidharan, G. N. Frantziskonis, Evolution of internal strain in austenite phase during thermally induced martensitic phase transformation in NiTi shape memory alloys, *Computational Materials Science* 133 (2017) 52–59. doi:[10.1016/j.commatsci.2017.03.012](https://doi.org/10.1016/j.commatsci.2017.03.012).
- [36] H. Tang, Y. Zhang, Q.-J. Li, H. Xu, Y. Wang, Y. Wang, J. Li, High accuracy neural network interatomic potential for NiTi shape memory alloy, *Acta Materialia* 238 (2022) 118217. doi:[10.1016/j.actamat.2022.118217](https://doi.org/10.1016/j.actamat.2022.118217).
- [37] J. Vandermause, A. Johansson, Y. Miao, J. J. Vlassak, B. Kozinsky, Phase discovery with active learning: Application to structural phase transitions in equiatomic NiTi, 2024. [arXiv:2401.05568](https://arxiv.org/abs/2401.05568).
- [38] Materials Data on TiNi by Materials Project, Technical Report mp-571, Lawrence Berkeley National Lab. (LBNL), Berkeley, CA (United States). LBNL Materials Project, 2020. doi:[10.17188/1276044](https://doi.org/10.17188/1276044).
- [39] Z. Wu, J. W. Lawson, Theoretical investigation of phase transitions in the shape memory alloy NiTi, *Physical Review B* 106 (2022) L140102. doi:[10.1103/PhysRevB.106.L140102](https://doi.org/10.1103/PhysRevB.106.L140102).

## CRediT author statement

S.B: Conceptualization, Formal Analysis, Investigation, Methodology, Software, Visualisation, Writing—original draft.

## Reproducibility and Data Availability

This study was carried out using the reproducibility software [show your work!](#)<sup>[18]</sup>, which leverages continuous integration to programmatically download the data from [zenodo.org](#)(if needed), create the figures, and compile the manuscript. Each figure caption contains two links: one to the dataset stored on zenodo used in the corresponding figure, and the other to the script used to make the figure (at the commit corresponding to the current build of the manuscript). The git repository associated to this study is publicly available at [https://github.com/stefanbringuier/SMA\\_Phonons\\_GNNIP](https://github.com/stefanbringuier/SMA_Phonons_GNNIP) and allows anyone to re-build the entire manuscript.

## Acknowledgements

The author would like to thank Prof. Venkateswara Manga at the University of Arizona for fruitful discussions.

## Appendix A. Appendix

*Appendix A.1. Workflow Reproducibility*

*Appendix A.2. NiTi: Ground State Structures*

Table A.2: Equilibrium structures for NiTi.

Structure	Model	Unit Cell					
		<i>a</i> (Å)	<i>b</i> (Å)	<i>c</i> (Å)	$\alpha$ (°)	$\beta$ (°)	$\gamma$ (°)
B2 (221)	Mutter	3.010	3.010	3.010	90.00	90.00	90.00
					x	y	z
					Ni	0.0000	0.0000
	Zhong	0.5000	0.5000	0.5000			
		3.011	3.011	3.011	90.00	90.00	90.00
					x	y	z
	Ko	0.5000	0.5000	0.5000	Ni	0.0000	0.0000
		2.999	2.999	2.999			
					Ti	0.0000	0.0000
M3GNet	M3GNet	3.006	3.006	3.006	90.00	90.00	90.00
					x	y	z
					Ni	0.0000	0.0000
	CHGNet	0.5000	0.5000	0.5000			
		3.005	3.005	3.005	90.00	90.00	90.00
					x	y	z
MACE	MACE	3.004	3.004	3.004	90.00	90.00	90.00
					x	y	z
					Ni	0.0000	0.0000
	CHGNet	0.5000	0.5000	0.5000			
		3.005	3.005	3.005	90.00	90.00	90.00
					x	y	z

Table A.2: Equilibrium structures for NiTi. (Continued)

Structure (Spacegroup #)	Unit Cell						
	Model	$a$ (Å)	$b$ (Å)	$c$ (Å)	$\alpha$ (°)	$\beta$ (°)	$\gamma$ (°)
B19P (11)	Mutter	2.992	4.004	4.881	90.00	107.79	90.00
				x	y	z	
				Ni	0.0871	0.2500	0.6751
				Ti	0.3588	0.2500	0.2167
	Zhong	2.993	4.001	4.871	90.00	107.39	90.00
				x	y	z	
Ko				Ni	0.0835	0.2500	0.6750
				Ti	0.3619	0.2500	0.2167
		3.149	3.760	4.984	90.00	108.42	90.00
				x	y	z	
				Ni	0.0718	0.2500	0.6436
				Ti	0.3503	0.2500	0.2006
M3GNet		2.905	4.010	4.952	90.00	107.04	90.00
				x	y	z	
				Ni	0.0779	0.2500	0.6561
				Ti	0.3513	0.2500	0.2024
	CHGNet	2.898	4.016	4.858	90.00	106.43	90.00
				x	y	z	
MACE				Ni	0.0744	0.2500	0.6601
				Ti	0.3556	0.2500	0.2003
		2.875	4.053	4.905	90.00	106.99	90.00
				x	y	z	
				Ni	0.0786	0.2500	0.6577
				Ti	0.3516	0.2500	0.2026

Table A.2: Equilibrium structures for NiTi. (Continued)

Structure (Spacegroup #)	Unit Cell						
	Model	$a$ (Å)	$b$ (Å)	$c$ (Å)	$\alpha$ (°)	$\beta$ (°)	$\gamma$ (°)
B19 (51)	Mutter	4.044	2.919	4.448	90.00	90.00	90.00
					x	y	z
				Ni	0.2500	0.0000	0.7919
				Ti	0.2500	0.5000	0.2816
	Zhong	4.038	2.916	4.462	90.00	90.00	90.00
				x	y	z	
				Ni	0.2500	-0.0000	0.7947
				Ti	0.2500	0.5000	0.2829
	Ko	4.275	2.809	4.502	90.00	90.00	90.00
				x	y	z	
				Ni	0.2500	0.0000	0.8296
				Ti	0.2500	0.5000	0.2992
M3GNet	M3GNet	4.258	2.906	4.395	90.00	90.00	90.00
				x	y	z	
				Ni	0.2500	-0.0000	0.8156
				Ti	0.2500	0.5000	0.2812
	CHGNet	4.205	2.867	4.501	90.00	90.00	90.00
				x	y	z	
				Ni	0.2500	-0.0000	0.8160
				Ti	0.2500	0.5000	0.2794
	MACE	4.233	2.815	4.539	90.00	90.00	90.00
				x	y	z	
				Ni	0.2500	0.0000	0.8215
				Ti	0.2500	0.5000	0.2840

Table A.2: Equilibrium structures for NiTi. (Continued)

Structure (Spacegroup #)	Model	Unit Cell					
		<i>a</i> (Å)	<i>b</i> (Å)	<i>c</i> (Å)	$\alpha$ (°)	$\beta$ (°)	$\gamma$ (°)
BCO (63)	Mutter	2.992	9.296	4.004	90.00	90.00	90.00
					x	y	z
					Ni	0.0000	0.0875
					Ni	0.5000	0.5875
					Ti	-0.0000	0.3583
	Zhong	2.993	9.303	4.001	90.00	90.00	90.00
					x	y	z
					Ni	-0.0000	0.0874
					Ni	0.5000	0.5874
					Ti	-0.0000	0.3581
	Ko	3.149	9.458	3.760	90.00	90.00	90.00
					x	y	z
					Ni	0.0000	0.0718
					Ni	0.5000	0.5718
					Ti	0.0000	0.3503
	M3GNet	2.905	9.470	4.010	90.00	90.00	90.00
					x	y	z
					Ni	-0.0000	0.0781
					Ni	0.5000	0.5781
					Ti	-0.0000	0.3512
	CHGNet	2.898	9.316	4.017	90.00	90.00	90.00
					x	y	z
					Ni	0.0000	0.0801
					Ni	0.5000	0.5801
					Ti	0.0000	0.3503
	MACE	2.875	9.382	4.053	90.00	90.00	90.00
					x	y	z
					Ni	0.0000	0.0789
					Ni	0.5000	0.5789
					Ti	0.0000	0.3513



### Appendix A.3. Phonon Calculation Configurations

The code used to generate the phonon configuration settings for each potential mode and structure are shown the table below. Settings are used for both NiTi and PtTi systems.

```
def get_phonon_config(structure_name, potential):
    """Settings for the phonon calculations

    - supercell
    - atomic displacement (angstrom)
    - q-points along band path

    Settings have been manually calibrated.
    """

    # Supercell, displacement (ang.), band path points
    configurations = {
        "B2": {
            "Mutter": ((8, 8, 8), 0.0935, 200),
            "Zhong": ((8, 8, 8), 0.0935, 200),
            "Ko": ((8, 8, 8), 0.01, 200),
            "Kavousi": ((8, 8, 8), 0.01, 200),
            "Kim": ((8, 8, 8), 0.01, 200),
            "M3GNet": ((8, 8, 8), 0.010, 200),
            "CHGNet": ((8, 8, 8), 0.030, 200),
            "MACE": ((8, 8, 8), 0.010, 200),
            "ALIGNN": ((6, 6, 6), 0.050, 200),
            "DeepMD": ((8, 8, 8), 0.03, 200),
            "GPAW": ((2, 2, 2), 0.03, 200),
        },
        "B19": {
            "Mutter": ((7, 9, 7), 0.05, 200),
            "Zhong": ((7, 9, 7), 0.05, 200),
            "Ko": ((7, 9, 7), 0.03, 200),
            "Kavousi": ((7, 9, 7), 0.03, 200),
            "Kim": ((7, 9, 7), 0.03, 200),
            "M3GNet": ((7, 9, 7), 0.05, 200),
            "CHGNet": ((6, 8, 6), 0.05, 200),
            "MACE": ((7, 9, 7), 0.05, 200),
            "ALIGNN": ((5, 7, 5), 0.05, 200),
            "DeepMD": ((7, 9, 7), 0.05, 200),
        },
        "B19P": {
            "Mutter": ((8, 6, 4), 0.05, 200),
            "Zhong": ((8, 6, 4), 0.05, 200),
            "Ko": ((8, 6, 4), 0.01, 200),
            "Kavousi": ((8, 6, 4), 0.01, 200),
        }
    }
```

```

        "Kim": ((8, 6, 4), 0.01, 200),
        "M3GNet": ((8, 6, 4), 0.05, 200),
        "CHGNet": ((8, 6, 4), 0.05, 200),
        "MACE": ((8, 6, 4), 0.05, 200),
        "ALIGNN": ((7, 5, 3), 0.05, 200),
        "DeepMD": ((8, 6, 4), 0.05, 200),
    },
    "BCO": {
        "Mutter": ((8, 4, 6), 0.05, 200),
        "Zhong": ((8, 4, 6), 0.05, 200),
        "Ko": ((8, 4, 6), 0.05, 200),
        "Kavousi": ((8, 4, 6), 0.05, 200),
        "Kim": ((8, 4, 6), 0.05, 200),
        "M3GNet": ((8, 4, 6), 0.05, 200),
        "CHGNet": ((8, 4, 6), 0.05, 200),
        "MACE": ((8, 4, 6), 0.05, 200),
        "ALIGNN": ((5, 2, 3), 0.05, 200),
        "DeepMD": ((8, 4, 7), 0.05, 200),
    },
}

# Validate structure_name and potential_key
if (
    structure_name not in configurations
    or potential not in configurations[structure_name]
):
    raise ValueError(
        f"Configuration not found for structure '{
            ↪ structure_name}' and potential '{potential_key}'"
        ↪ "
    )

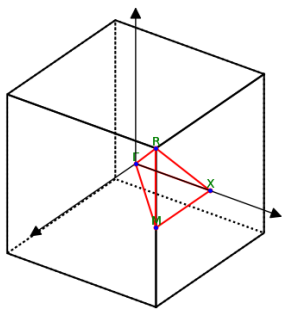
# Retrieve configuration
return configurations[structure_name][potential]

```

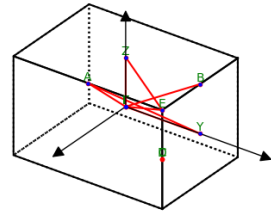


#### *Appendix A.4. Irreducible Brillouin Zones*

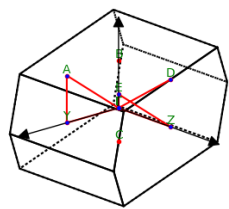
The irreducible Brillouin zones for the the different crystals investigated in this study are provided below. The high-symmetry points are indicated. Additionally the coordinates of the high-symmetry points in the IBZ are shown in the tables below. In Ref. xxx the specific implementation of the band path sampling and definitions are provided.



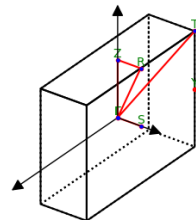
(a)



(b)



(c)



(d)

Figure A.13: The irreducible Brillouin zones for  $B2(\#221)$ ,  $B19(\#51)$ ,  $B19'(\#11)$ , and  $BCO(\#63)$  crystal structures

Point	Coordinates
G	0.0, 0.0, 0.0
M	0.5, 0.5, 0.0
R	0.5, 0.5, 0.5
X	0.0, 0.5, 0.0

Table A.3: Special points sampled in the irreducible Brillouin Zone for space group 221

Point	Coordinates
G	0.0, 0.0, 0.0
Y	0.0, 0.5, 0.0
Z	0.0, 0.0, 0.5
B	0.0, 0.5, 0.5
C	0.5, 0.5, 0.0
A	0.5, 0.0, 0.5
D	0.5, 0.5, 0.0
E	0.5, 0.5, 0.5

Table A.4: Special points sampled in the irreducible Brillouin Zone for space group 51

Point	Coordinates
G	0.0, 0.0, 0.0
Y	0.5, 0.0, 0.0
Z	0.0, 0.5, 0.0
B	0.0, 0.0, 0.5
C	0.5, 0.5, 0.0
A	0.5, 0.0, 0.5
D	0.0, 0.5, 0.5
E	0.5, 0.5, 0.5

Table A.5: Special points sampled in the irreducible Brillouin Zone for space group 11

Point	Coordinates
G	0.0, 0.0, 0.0
Y	-0.5, 0.5, 0.0
Z	0.0, 0.0, 0.5
S	0.0, 0.5, 0.0
R	0.0, 0.5, 0.5
T	-0.5, 0.5, 0.5

Table A.6: Special points sampled in the irreducible Brillouin Zone for space group 63